Journal of Sound and Vibration 329 (2010) 1215–1226

Contents lists available at ScienceDirect

Journal of Sound and Vibration

journal homepage: www.elsevier.com/locate/jsvi

Rapid Communication

Investigations of a nonlinear energy harvester with a bistable potential well

B.P. Mann *, B.A. Owens

Department of Mechanical Engineering & Material Science, Duke University, Durham, NC 27708, USA

ARTICLE INFO

Article history:
Received 8 September 2009
Received in revised form
31 October 2009
Accepted 27 November 2009
Handling Editor: M.P. Cartmell
Available online 21 December 2009

ABSTRACT

This paper investigates a nonlinear energy harvester that uses magnetic interactions to create an inertial generator with a bistable potential well. The motivating hypothesis for this work was that nonlinear behavior could be used to improve the performance of an energy harvester by broadening its frequency response. Theoretical investigations study the harvester's response when directly powering an electrical load. Both theoretical and experimental tests show that the potential well escape phenomenon can be used to broaden the frequency response of an energy harvester.

1. Introduction

Recent advancements in the microelectronics industry have enabled a reduction in the power consumed by MEMS devices [1,2]. This has motivated many works that investigate meeting the need for remote power by scavenging energy from the environment [3]. While solar, chemical and thermal methods are sometimes viable, many have recognized the abundance of vibration as a potential source of energy [1,4–10]; thus, extracting energy from an inertial generator interacting with its environment has become a promising area of inquiry. For instance, Ref. [11] describes several works that consider using ambient vibration to power wireless sensor networks for bridges, buildings, or aircraft and the powering of body-worn or implanted electronics with human motion.

Starting with the work of Williams et al. [10], the focus has primarily been on inertial generators with linear behavior. In addition, most works only consider single-frequency excitation, unless the device complexity was increased to include additional degrees of freedom, e.g. see Ref. [7]. A primary limitation of inertial generators with linear performance is that they only perform well for a narrow band of frequencies; any variation in the excitation frequencies will greatly reduce device's ability to harvest energy. This also provides an implementation challenge, since it is typically difficult to match the linear resonance of a fabricated device to an environmental frequency [7,12]. Recent efforts have attempted to overcome this shortcoming of linear devices with passive or active methods to tune the device's resonance and/or widening of the bandwidth by adding many oscillators [7,13]. The present work differs from past investigations by offering an alternative paradigm to frequency matching and linear resonance. More specifically, we investigate a nonlinear generator and the use of potential well escapes as a phenomenon for energy harvesting.

The present article describes the design and performance of an electromagnetic-induction energy generator that directly powers an electrical load. The generator contains a moving magnet that is suspended in reference to an external housing with magnetic repulsion [5,12]. When an external source accelerates the device's housing, the proof mass begins

---

* Corresponding author.
E-mail address: brian.mann@duke.edu (B.P. Mann).

0022-460X/$ - see front matter © 2009 Elsevier Ltd. All rights reserved.
doi:10.1016/j.jsv.2009.11.034

to oscillate and convert mechanical energy into electrical energy via electromagnetic-induction. A novel feature of the present study is the exploitation of nonlinear interactions to tailor the generator's bistable potential well.

The work of this paper is organized as follows. The next section provides a physical description of the device. This is followed by a section that describes the modeling efforts that were used to design the nonlinear generator. Theoretical results show the presence of co-existing solutions and a broadening in the harvester's frequency response for some levels of base excitation. Finally, the paper concludes with a series of experimental results that confirm that the potential well escape phenomenon can be used to broaden the frequency spectrum of an energy harvester.

2. Experimental apparatus

A schematic of the experimental system is shown in Fig. 1. The device consisted of a series of magnets that were positioned to make the system bistable. For instance, the top and bottom magnets were mechanically attached to a top and bottom cap that were inserted into a tube that allowed the half-spacing *d* (shown in Fig. 1 a) to be adjusted. A center magnet was placed between these magnets and oriented to repel both outer magnets—thereby suspending the oscillating center magnet within the tube [4,12]. Four magnets were placed symmetrically around the tube's midpoint; the purpose of these magnets was to repel the center magnet away from the midpoint and to make the inertial generator bistable (see Figs. 1 a and b).

Fig. 1 c shows an adaptation used to minimize mechanical dissipation. Specifically, a tensioned guide wire was used in combination with two PTFE (polytetrafluoroethylene) inserts. These inserts were designed to contact the guide wire only at the location furthest from the center magnet; this reduced the frictional losses by lowering the normal force that results from the interaction torques of the surrounding magnets. Fig. 1 d provides a schematic for the electrical circuit that was used in the studies that follow. This simple circuit contains the coil's inductance L and internal resistance R_i along with a resistive load R_L.

3. Energy generator model

This section derives a theoretical model for the nonlinear generator. The mathematical models derived here are later used, in Section 4, to study the power delivered to an electrical load.

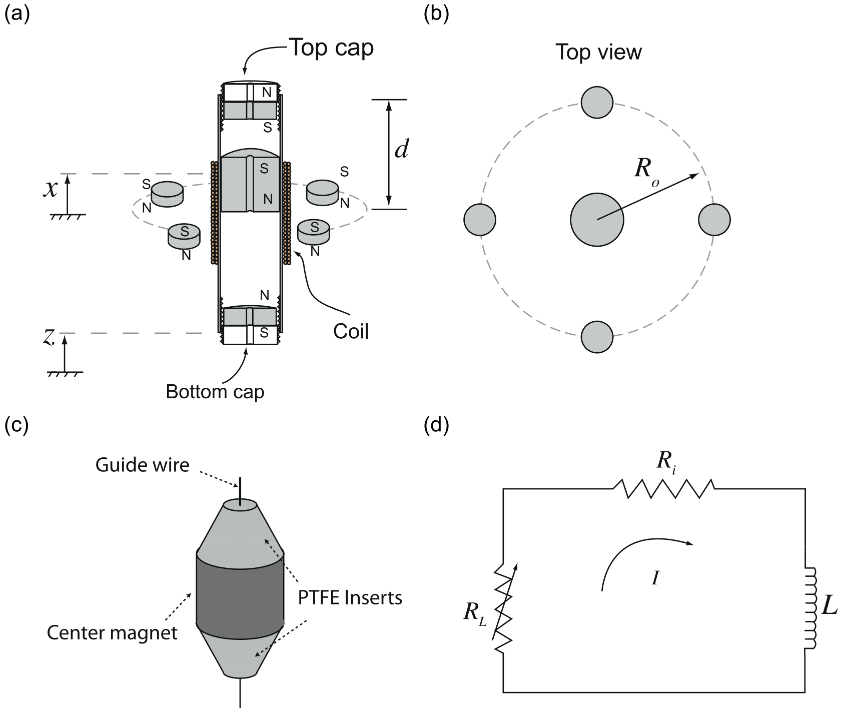

Fig. 1. Illustrations of the nonlinear generator (schematics (a) and (b)), the inserts used to reduce mechanical damping (c), and a schematic of the coupled electrical circuit (d).

3.1. Nonlinear generator model

To account for the interactions between the oscillating and fixed magnets, the potential energy and force expressions were derived from a dipole model (see Refs. [14–17]); this section describes the salient features of the derivation by first introducing the expressions for two interacting magnets and then applying these expressions to multiple magnets. The magnetic flux density or $\mathbf{B}$—field at the location $\mathbf{r}_p$ due to a magnet located at $\mathbf{r}_s$ is defined by

$$\mathbf{B} = -\frac{\mu_0}{4\pi}\nabla\frac{\mathbf{m}_s \cdot \mathbf{r}_{p/s}}{|\mathbf{r}_{p/s}|^3}, \tag{1}$$

where $\mu_0 = 4\pi \times 10^{-7}$ H/m is the permeability of free space, ∇ is the vector gradient, $\mathbf{r}_{p/s} = \mathbf{r}_p - \mathbf{r}_s$ is a vector to the point of interest (the point $P(x,y,z)$) with respect to the location of the source magnet, and $|\mathbf{r}_{p/s}|$ is the distance between the two magnets. The magnetic moment of the source magnet, which is located at $\mathbf{r}_s$, is given by $\mathbf{m}_s = \mathbf{M}_s \upsilon_s$, where $\mathbf{M}_s$ and υ_s are the magnetization and volume of the source magnet, respectively. The potential energy of the magnet at $\mathbf{r}_p$ in the field generated by the magnet at $\mathbf{r}_s$ is

$$U = -\mathbf{m}_p \cdot \mathbf{B}, \tag{2}$$

where $\mathbf{m}_p$ is the magnetic moment of the magnet located at $\mathbf{r}_p$. An expression for the interaction force between the magnets can be obtained by taking the gradient of Eq. (2).

The potential energy of the center magnet due to the interactions with the other six magnets can be obtained using Eqs. (1) and (2). For this purpose, we introduce the parameters υ_c, υ_o, and υ_t to define the volumes of the center magnet, each of the outer-four magnets, and the identical top and bottom magnets, respectively; the corresponding magnetization amplitudes of these magnets are defined by M_c, M_o, and M_t, where the subscripts match those applied to the magnet volumes. Introducing d as the half-spacing between the top and bottom magnets (see Fig. 1 a) the expression for the potential energy becomes

$$U = \frac{\mu_0 M_c \upsilon_c}{2\pi}\left[\upsilon_t M_t\left(\frac{1}{(d+y)^3} + \frac{1}{(d-y)^3}\right) - \frac{M_o \upsilon_o N}{2}\left(\frac{y^2}{(y^2+R_o^2)^{5/2}} - \frac{1}{(y^2+R_o^2)^{3/2}}\right)\right], \tag{3}$$

where $y = x - z$ is the relative position of the center magnet with respect to the device's outer housing and the number of outer-ring magnets was $N = 4$. These magnets were located a radial distance R_o from the central axis and on the plane of symmetry that divides the top from the bottom half of the device. An expression for the restoring forces was obtained from the derivative of the potential energy with respect to y. For completeness, we have listed this expression below

$$F_m(y) = \frac{\mu_0 M_c \upsilon_c}{2\pi}\left[\upsilon_t M_t\left(\frac{3}{(d-y)^4} - \frac{3}{(d+y)^4}\right) - \frac{M_o \upsilon_o N}{2}\left(\frac{5y}{(y^2+R_o^2)^{5/2}} - \frac{5y^3}{(y^2+R_o^2)^{7/2}}\right)\right]. \tag{4}$$

The governing equations for the energy generator directly powering a resistive load, as shown in Fig. 1, are given by

$$L\dot{I} + (R_L + R_i)I + \gamma\dot{y} = 0, \tag{5a}$$

$$m\ddot{y} + c\dot{y} + F_m(y) - \gamma I = -m\ddot{z}, \tag{5b}$$

where an overdot indicates a derivate with respect to time, m is the mass of the center magnet, c is a constant used to describe the mechanical dissipation, $\ddot{z}$ is the base acceleration, I is the electrical current, L is the inductance of the coil, and γ is a transducer constant, which can be derived from Faraday's law of induction, that couples the mechanical and electrical systems.

Eqs. (3)–(5b) were used in conjunction with the magnet characteristics, which have been listed in Table 1, to generate the bifurcation diagram and potential energy curves of Fig. 2 when $d = 106$ mm. This bifurcation diagram shows the changes in the static equilibria y_e, the equilibria of Eqs. (5a) and (5b), for changes in the location of the outer ring of magnets. Furthermore, the bifurcation diagram shows that changes in R_o give rise to a supercritical pitchfork bifurcation; this reveals the values of R_o where the generator becomes bistable. Since the stable equilibria can also be obtained from the local minima of the potential energy curve [18], plotting Eq. (3) can provide a visual indicator of the stable equilibria. For instance, Figs. 2 b and c show a monostable and bistable system, respectively; the bistable case of Fig. 2 c was generated using $R_o = 38$ mm, which was the same R_o value used in the experimental device.

Table 1
Magnetization and magnet dimensions with an inner diameter d_i, outer diameter d_o, and length ℓ.

Magnet	M (A/m)	d_i (mm)	d_o (mm)	ℓ (mm)
Center	1.0504 × 106	6.35	19.05	19.05
Outer ring	1.1777 × 106	0	9.52	9.52
Top/bottom	1.0504 × 106	6.35	19.05	6.35

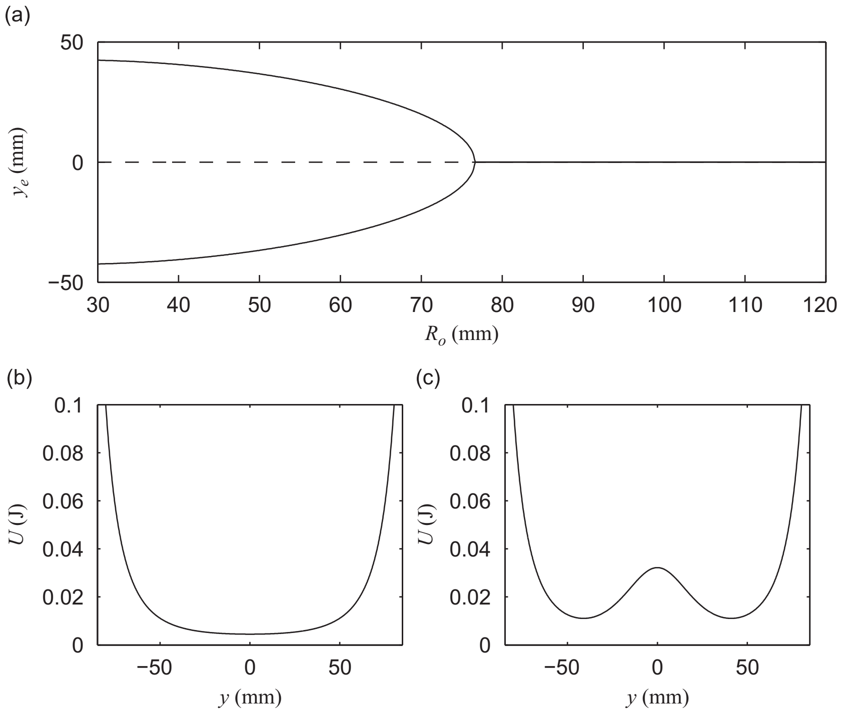

Fig. 2. Bifurcation diagram (a) and potential energy curves (b)–(c) for various radial spacings of the outer ring of magnets. Stable (solid line) and unstable (dashed) equilibria are marked in graph (a). The parameters of Table 1 were used along with $d = 106$ mm and $R_o = 100$ mm for graph (b) and $R_o = 38$ mm for graph (c).

Table 2
Parameters used in the studies of Section 4.

Parameter	Value
m (Kg)	35.6×10^{-3}
μ (N m/s)	0.32
L (H)	76×10^{-3}
R_i (Ω)	127
γ (A s/m)	5

For the convenience of the discussion that follows, Eqs. (5a) and (5b) have been written in the following condensed form:

$$L\dot{I} + IR + \gamma\dot{y} = 0, \tag{6a}$$

$$\ddot{y} + 2\mu\dot{y} + \frac{1}{m}F_m(y) - \hat{\gamma}I = -\ddot{z}, \tag{6b}$$

where $R = R_L + R_i$, $2\mu = c/m$, and $\hat{\gamma} = \gamma/m$. Since we were interested in the frequency response of the system, it was useful to know the natural frequency for the theoretical device. To determine the natural frequency, we derived a linear stiffness of $k = 36.9$ N/m by evaluating the gradient of $F_m(y)$ at the equilibrium position $y_e = 41.1$ mm. Next, this was divided by the mass, given in Table 2 to obtain the linear natural frequency $\omega = \sqrt{k/m} = 32.17$ rad/s or 5.12 Hz.

4. Theoretical investigations

This section investigates the response behavior of the nonlinear harvester and the power delivered to an electrical load. Since the generator directly powered a resistive load, the instantaneous power delivered to the electrical load was given by $P = I^2R_L$. The investigations that follow consider single-frequency excitation $\ddot{z} = A\cos\theta(t)$, where A is the acceleration amplitude and $\dot{\theta}(t) = \Omega(t)$ is the excitation frequency in rad/s, to investigate the harvester's response. The next section shows results for exciting the base with a constant A, but allowing the excitation frequency to slowly increase or decrease. This is followed by a series of results that hold Ω constant while slowly changing A.

4.1. *Frequency response*

Broadening the range of frequencies from which a relatively large amount of energy can be extracted is of considerable interest in energy harvesting. To provide insight into the harvester's capability to achieve this goal, numerical simulations were performed on Eqs. (6a) and (6b) for linearly increasing and decreasing excitation frequencies. However, before discussing the response and performance of the harvester, we first explain how the model parameters were chosen for the numerical studies. More specifically, our intent was to use parameters that were representative of the experimental system.

A cylindrical coil with $n = 2000$ winds of enamel-coated magnet wire was used in the experimental studies that follow; the coil's dimensions were $r_i = 15.9\,\text{mm}$ and $\ell_c = 50.8\,\text{mm}$ for the inner radius and height, respectively. If the coil is approximated as a long solenoid, the expression from Ref. [16] can be used to estimate the inductance $L \approx \mu_0(n^2\pi r_i^2/\ell_c) = 78 \times 10^{-3}\,\text{H}$. This agrees closely with the experimentally measured value of $L = 76 \times 10^{-3}\,\text{H}$, which was used in the numerical studies. Simulation studies also used $R_L = 1217\,\Omega$ and the experimentally measured values for R_i and γ; these values, along with the measured mass and estimated damping of the experimental system have been listed in Table 2. In addition, the terms that describe the magnetic restoring forces were also required; thus the magnet characteristics of Table 1 were used in combination with $d = 106\,\text{mm}$ and $R_o = 38\,\text{mm}$ to determine the magnetic forces.

The graphs of Figs. 3–5 show an array of frequency responses that were predicted for different levels of base excitation. More specifically, the forward (or linearly increasing) frequency sweep results of Fig. 3 show the time series for the magnet displacement and the circuit current along with their respective stroboscopic points, i.e. each time series sampled at $\lfloor \theta(t)/2\pi \rfloor$ where $\theta(t) = (\Omega_0 + \frac{1}{2}\Omega_r t)t$ is a function of the sweep rate Ω_r, start frequency Ω_0, and time. While the time series shows the amplitude of each state at a given frequency, the stroboscopic samples of these states reveals the periodicity of these responses with respect to the excitation frequency, e.g. see periodic responses in Figs. 3 a and b or chaotic responses in the middle of the frequency range for Figs. 3 e and f.

The forward sweep cases of Fig. 3 can also be compared with the reverse sweep (or linearly decreasing) cases of Fig. 4. For instance, for small excitation levels, the harvester responds identically for forward and reverse frequency sweeps with a resonant peak near the linear natural frequency. In contrast, the responses at larger levels of excitation reveal a broadening of the peak response, hysteresis in the frequency responses, the presences of multiple attractors (co-existing solutions), and chaotic attractors. Furthermore, the largest level of excitation also unveils a significant broadening in the frequency response.

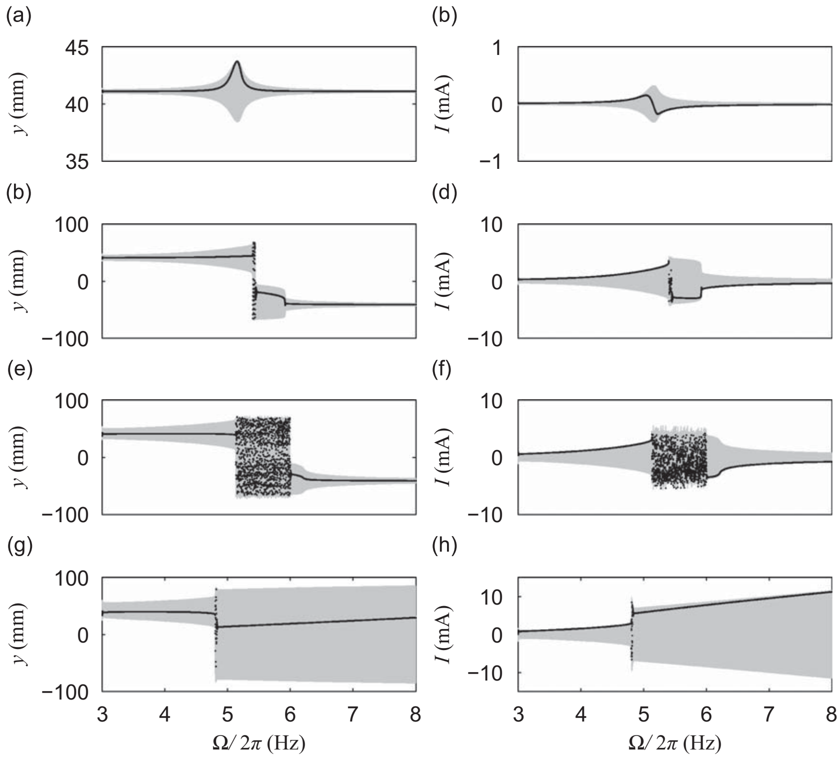

Fig. 3. Forward frequency sweep responses of the center magnet displacement (left column) and the current (right column) for different base excitations. Both the continuous time series (shaded) and stroboscopic samples (black dots) are shown. The parameters of Table 2 were used along with the following base accelerations: (a,b) $A = 0.1\,\text{m/s}^2$, (c,d) $A = 3\,\text{m/s}^2$, (e,f) $A = 6\,\text{m/s}^2$, and (g,h) $A = 10\,\text{m/s}^2$.

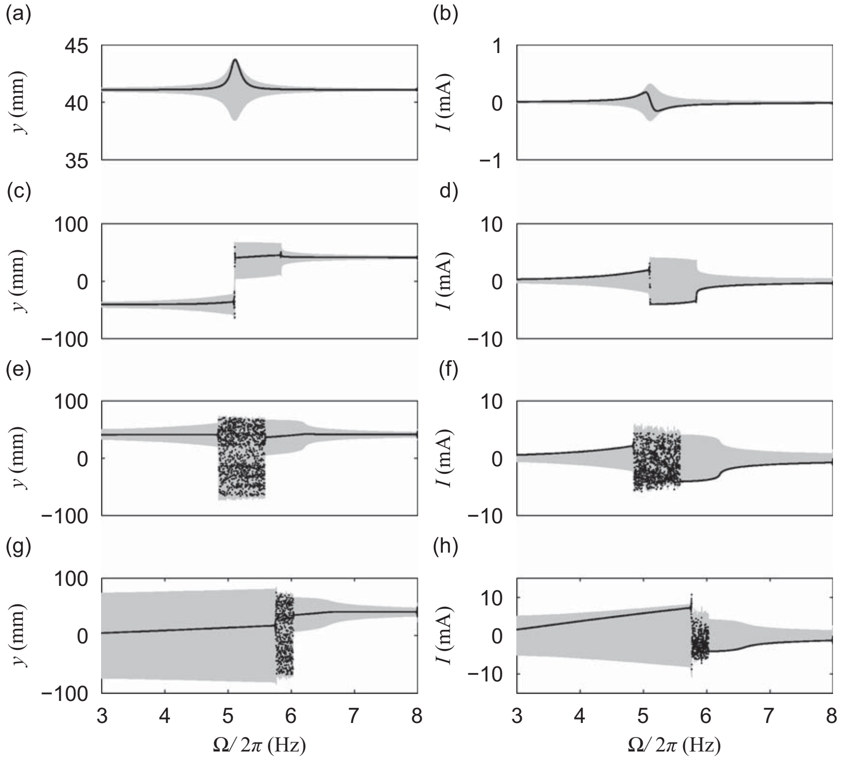

Fig. 4. Reverse frequency sweep responses of the center magnet displacement (left column) and the current (right column) for different base excitations. Both the continuous time series (shaded) and stroboscopic samples (black dots) are shown. The parameters of Table 2 were used along with the following base accelerations: (a,b) $A=0.1\,\mathrm{m/s^2}$, (c,d) $A=3\,\mathrm{m/s^2}$, (e,f) $A=6\,\mathrm{m/s^2}$, and (g,h) $A=10\,\mathrm{m/s^2}$.

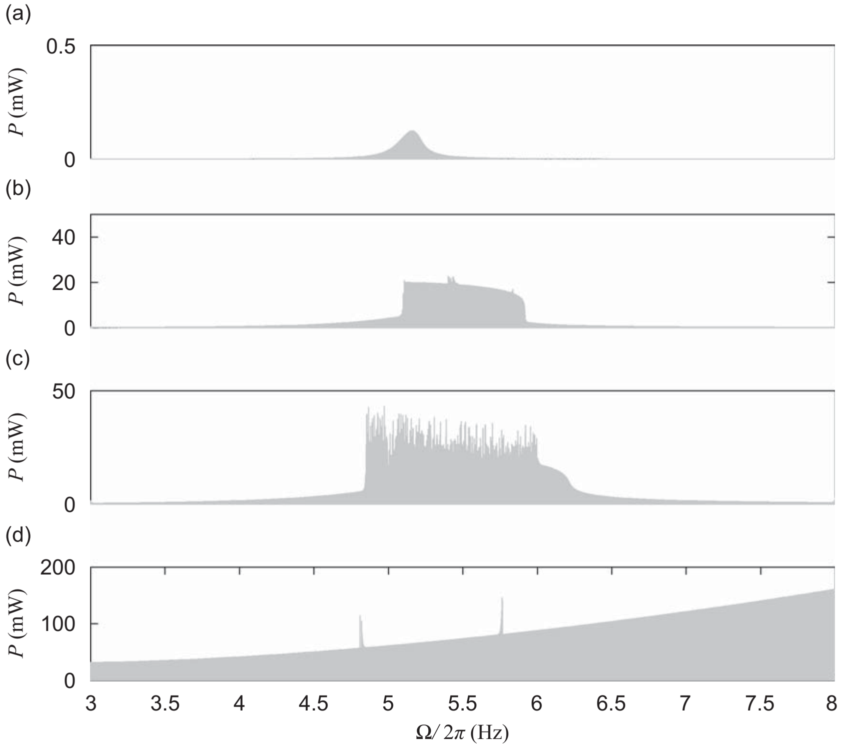

Fig. 5. Instantaneous power delivered to an electrical load for the forward and reverse frequency sweeps of Figs. 3 and 4. The parameters of Table 2 were used along with the following base accelerations: (a) $A=0.1\,\mathrm{m/s^2}$, (b) $A=3\,\mathrm{m/s^2}$, (c) $A=6\,\mathrm{m/s^2}$, and (d) $A=10\,\mathrm{m/s^2}$.

The frequency responses of the system can be used to ascertain the frequency dependence of the power delivered to an electrical load. In particular, the graphs of Fig. 5 provide the power over the range of frequencies that were studied in the previous two figures. For the lowest level of base excitation, the power graph shows a rather narrow peak near the natural frequency of the system. This type of response, which is reminiscent of classical linear behavior, no longer dominates the responses for increased levels of base excitation; instead, the frequency response begins to broaden for higher levels of base excitation.

4.2. Base excitation sweeps

This section describes the investigations performed to study the harvester's change in response for different levels of base excitation. More specifically, the numerical studies explored several cases where the base acceleration A was varied linearly, but the excitation frequency was held constant. A series of representative results, obtained with the same model parameters as those of Section 4.1, are shown in Figs. 6–8. As in the previous section, stroboscopic samples of the magnet displacement and current time histories have been overlaid onto the respective time series; however, the time series were sampled at the excitation period $T = 2\pi/\Omega$ since the excitation frequency was constant.

The forward amplitude sweeps of Fig. 6 provide a series of interesting results. While nearly linear behavior occurs for relatively small levels of base excitation, highly nonlinear behavior is observed as the excitation level is increased. For example, consider the case shown in Figs. 6 a and b. The harvester's response is initially periodic with oscillations that remain confined to a single potential well. Further increases in the excitation amplitude cause a potential well escape and trigger a chaotic response. However, the chaotic response does not persist; instead, the system's response returns to periodic motion at the highest levels of excitation. While similar types of complex bifurcations could be discussed in the remaining graphs, the authors would like to focus the reader on a certain observation; specifically, the energy level of the system abruptly jumps to a higher level after a potential well escape [19]. This is obvious from the jumps in both the magnet displacement and current that occur immediately after an escape.

The behavior of the forward sweeps of Fig. 6 can be directly contrasted with the responses in the reverse amplitude sweeps of Fig. 7. For instance, the forward sweeps exhibit periodic, subharmonic, and chaotic responses, but only periodic responses occurred during the reverse sweeps. Another comparison of interest is that more energetic responses were found in the regions of well-mixing behavior, i.e. regions where the oscillations traverse both potential wells [20–22]. One of the best examples of this shows up in cases (e) and (f) of both figures. Specifically, the magnet oscillations are still confined to a single potential well in the forward sweep at $4\,\mathrm{m/s^2}$, but the well-mixing behavior occurs $4\,\mathrm{m/s^2}$ in the

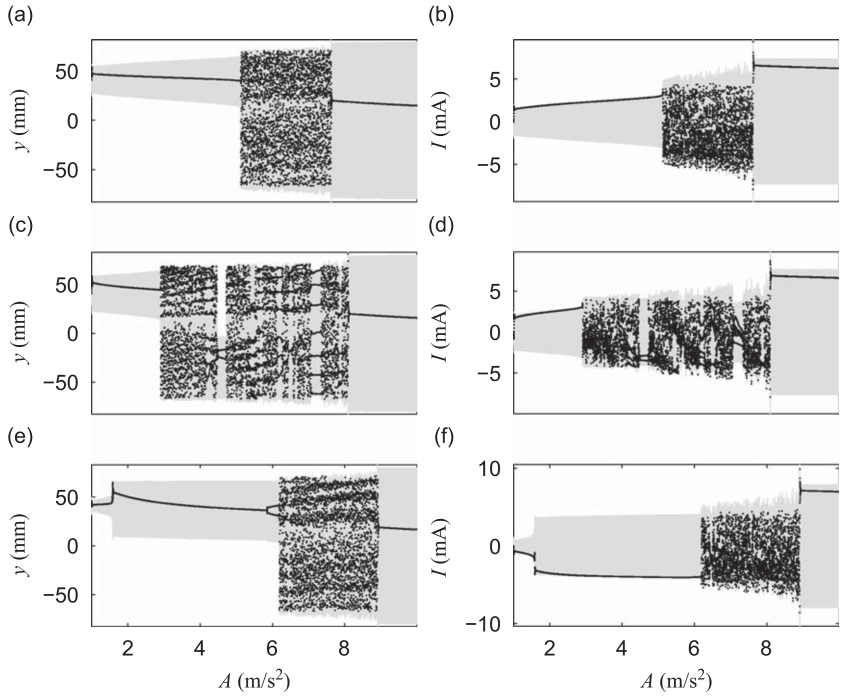

Fig. 6. Continuous (shaded) and periodically sampled (black dots) time histories of the magnet displacement (left column) and current responses (right column) when subjected to a slowly increasing excitation amplitude. Graphs used the magnet parameters of Table 1 when $R_o = 38\,\mathrm{mm}$, the harvester parameters of Table 2, $R_L = 1217\,\Omega$, and the following excitation frequencies: $\Omega/2\pi = 5.2\,\mathrm{Hz}$ for (a) and (b), $\Omega/2\pi = 5.4\,\mathrm{Hz}$ for (c) and (d), $\Omega/2\pi = 5.6\,\mathrm{Hz}$ for (e) and (f).

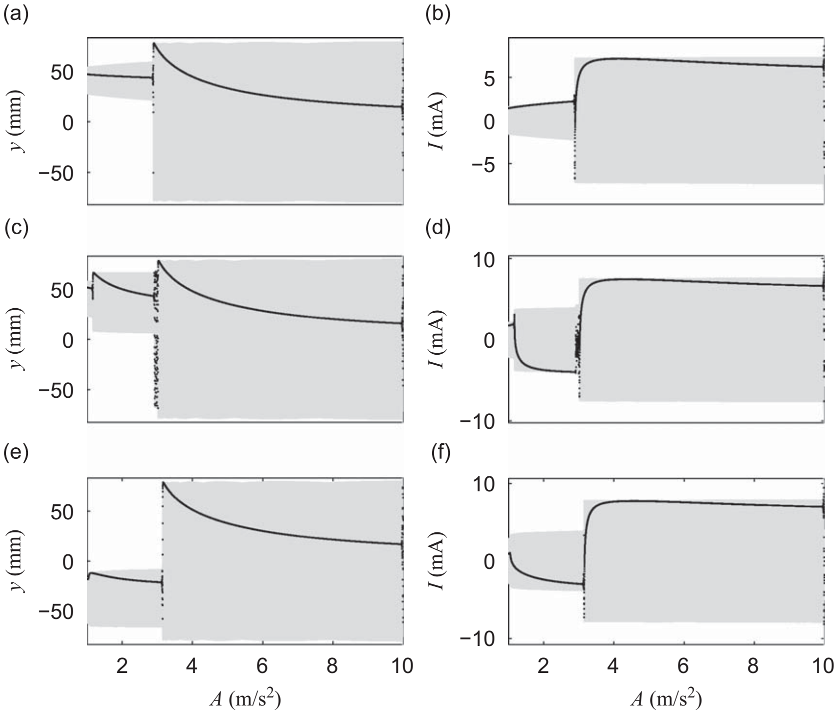

Fig. 7. Continuous (shaded) and periodically sampled (black dots) time histories of the magnet displacement (left column) and current responses (right column) when subjected to a slowly decreasing excitation amplitude. Graphs used the magnet parameters of Table 1 when $R_o = 38\,\text{mm}$, the harvester parameters of Table 2, $R_L = 1217\,\Omega$, and the following excitation frequencies: $\Omega/2\pi = 5.2\,\text{Hz}$ for (a) and (b), $\Omega/2\pi = 5.4\,\text{Hz}$ for (c) and (d), $\Omega/2\pi = 5.6\,\text{Hz}$ for (e) and (f).

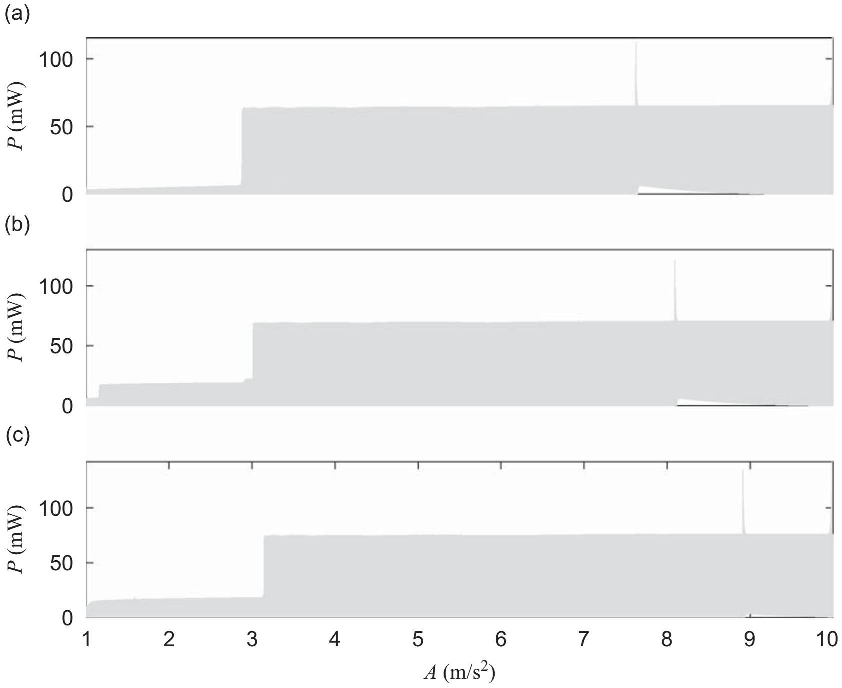

Fig. 8. Power delivered to the electrical load for each case of Fig. 6. Cases (a), (b), and (c) of the present figure provide the power for the top, middle, and bottom rows of Fig. 6, respectively.

reverse sweep. Since the current amplitude was higher for the reverse sweep, the power delivered to the electrical load was higher as well.

Fig. 8 shows power results for the cases studied in the previous two figures. These plots illustrate that a relatively large amount of power can be generated at low levels of base excitation—provided that the higher-energy attractor or response is obtained. In addition, it is interesting that the power does not appreciably increase for the higher levels of base excitation.

5. Experimental investigations

Fig. 9 shows a picture of the fabricated generator attached to the shaker table. The generator was held in a horizontal orientation to avoid the influence of gravity. As in Fig. 1, the generator's coil was wired to directly power a resistive load; the resistive load was set to $R_L = 150\,\Omega$ and the voltage drop across the resistive load was measured with a data acquisition system. Harmonic base excitation was applied by mounting the inertial generator to an air bearing shake table. To alleviate the possibility of magnetic field interference from the shaker, the attachment support was designed to distance the energy harvester away from the shaker base. During the experimental tests, the base acceleration was measured by mounting an accelerometer to the shake table.

5.1. Experimental trials

This section describes the experimental tests performed to compare experimental behavior with theoretical predictions. The experimental tests can be broadly separated into the performance of: (1) frequency sweeps or changes in the excitation frequency while holding all other experimental variables constant; and (2) excitation amplitude sweeps where the excitation amplitude was varied while holding the excitation frequency and all other variables constant.

The first series of experimental tests are shown in Fig. 10. This figure compares three forward (linear increasing) and reverse (linearly decreasing) frequency sweep tests. As shown theoretical results of Figs. 3 b and 4 b, at relatively low excitation levels, the frequency response of the system looks similar to the response of a linear system, i.e. no hysteresis in forward or reverse sweep responses and only a single periodic attractor at each excitation frequency. However, the results of Figs. 10 e and f show that an increase in excitation amplitude gives rise to multiple periodic attractors and hysteresis in the frequency response. Another interesting observation is that both the forward and reverse sweeps exhibit chaotic behavior near 6 Hz. As expected from the theoretical investigations, the experimental frequency response broadens at relatively higher levels of excitation. Perhaps this is most obvious from the power plots of Fig. 11, which overlay the power delivered during the forward and reverse sweeps.

Another array of experimental tests have been displayed in Fig. 12. This figure shows two amplitude sweeps or cases where the excitation frequency was held constant, but the amplitude of the base acceleration was linearly decreased. Below each amplitude sweep is a plot of the power delivered to the resistive load; these graphs show sharp increases in the

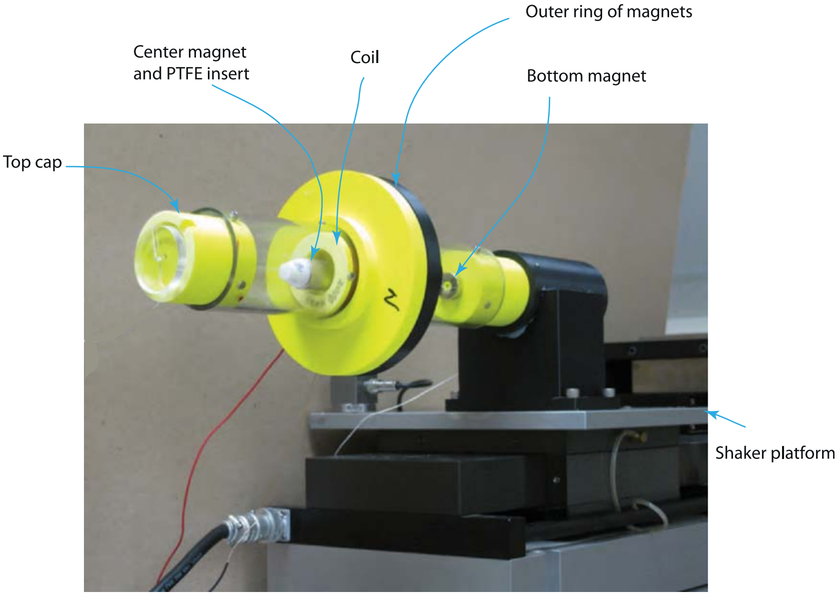

Fig. 9. Picture of the fabricated system that was used to investigate potential well escapes in a bistable energy harvester.

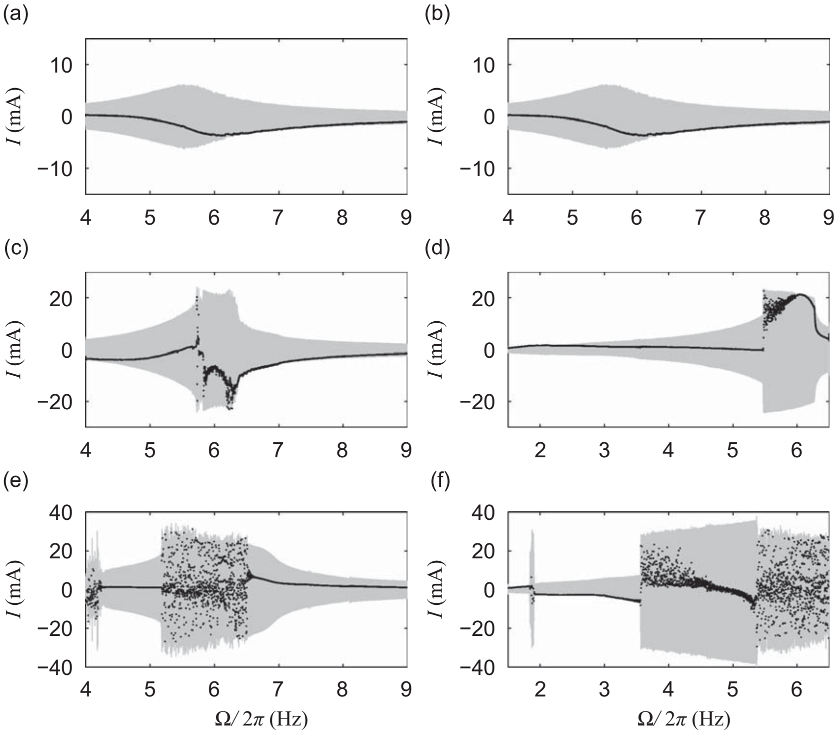

Fig. 10. Experimental forward (left column) and reverse (right column) frequency sweep responses when $R_L = 150\,\Omega$. Both the continuous time series (shaded) and stroboscopic samples (black dots) are shown. The following base accelerations were used: (a,b) $A = 5\,\mathrm{m/s^2}$, (c,d) $A = 6.7\,\mathrm{m/s^2}$, (e,f) $A = 10\,\mathrm{m/s^2}$.

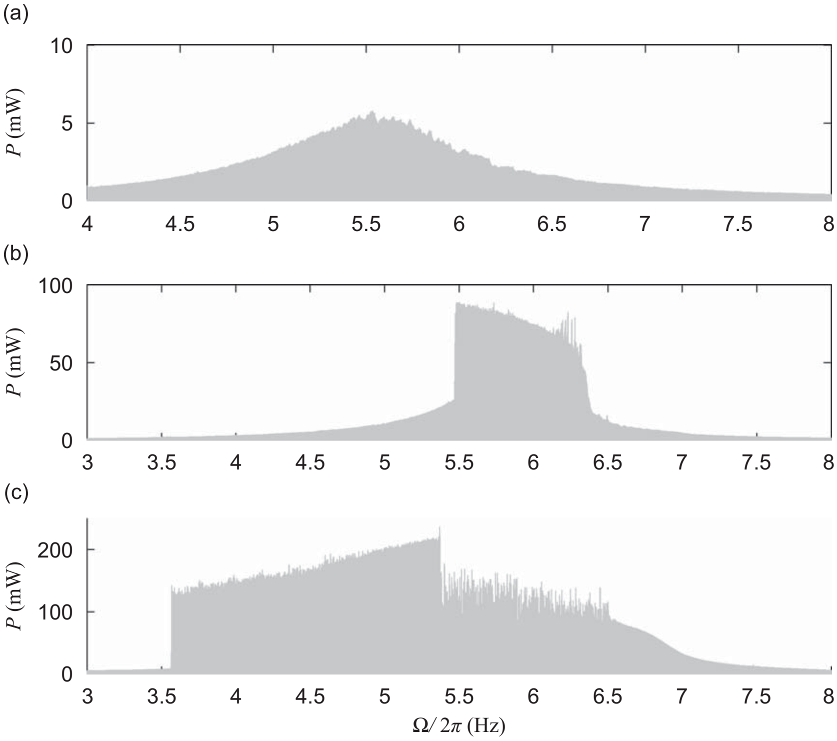

Fig. 11. Power delivered to an electrical load for the experimental frequency sweeps of Fig. 10. The following base accelerations were used: (a) $A = 5\,\mathrm{m/s^2}$, (b) $A = 6.7\,\mathrm{m/s^2}$, (c) $A = 10\,\mathrm{m/s^2}$.

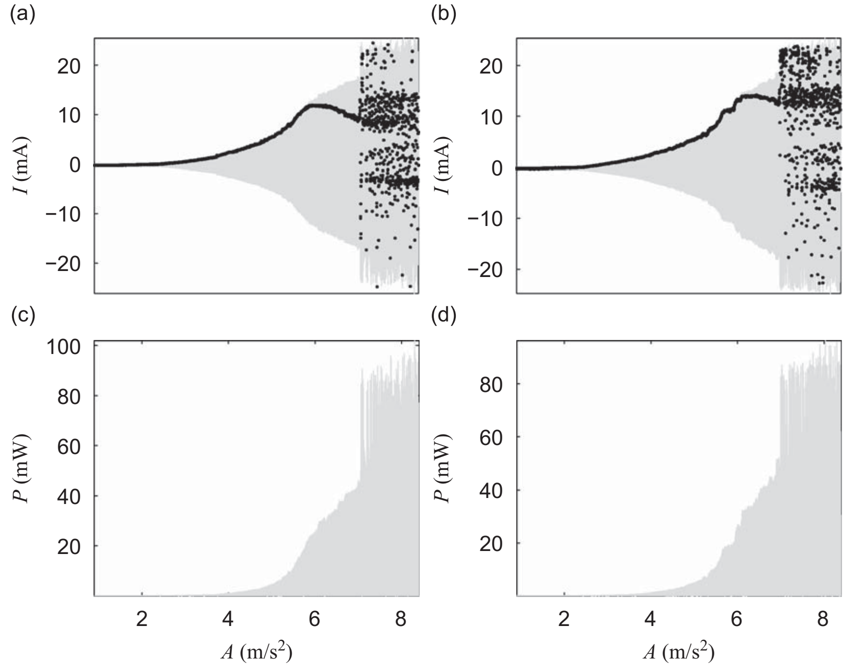

Fig. 12. Experimental current in the electrical circuit (top row) and power (bottom row) for a slowly decreasing excitation amplitude. Continuous time traces are shaded and once per forcing period samples are shown with black dots. Graphs (a) and (c) are for $\Omega/2\pi = 5.6$ Hz while graphs (b) and (d) are for $\Omega/2\pi = 5.8$ Hz.

power for the regions where well-mixing behavior was observed in laboratory and a chaotic response is shown in the figure.

6. Conclusions

This paper investigated an alternative paradigm to the standard approach applied in energy harvesting, i.e. frequency matching to the linear resonance. More specifically, our focus was on a nonlinear concept where the escape phenomenon was integrated into a prototype harvester. The paper introduced a mathematical model for the energy harvester that was used to tailor the potential wells and study the performance theoretically. Theoretical and experimental investigations reveal regions of coexisting solutions (higher and lower-energy responses) and hysteresis in the frequency and amplitude sweeps. The present investigations also reveal that a nonlinear generator, particularly one with a bistable potential well, can be used to broaden the frequency response.

The presence of multiple attractors provides an additional complication that is not observed in linear harvesters. Specifically, both higher and a lower-energy responses can coexists for the same parameter combinations. However, we note that the coupling between the electrical circuit and mechanical oscillations could be used to trigger a jump to the more desirable attractor; alternatively, we have perturbed the experimental system during testing to trigger jumps between the different attractors.

In summary, the present studies show that a nonlinear phenomenon—the escape from a potential well—can be used to broaden the frequency spectrum of an energy harvester. However, optimizing the performance of the nonlinear design was not attempted, as this is likely to present a formidable challenge. In addition, it is likely that many other nonlinear phenomena could also be used to achieve performance increases.

Acknowledgment

The author would like to acknowledge financial support from Dr. Ronald Joslin through an ONR Young Investigator Award.

References

[1] P. Glynne-Jones, M.J. Tudor, S.P. Beeby, N.M. White, An electromagnetic, vibration-powered generator for intelligent sensor systems, *Sensors and Actuators A* 110 (2004) 344–349.
[2] S. Roundy, P.K. Wright, J.M. Rabaey, *Energy Scavenging for Wireless Sensor Networks*, Springer, New York, 2003.

[3] S.P. Beeby, M.J. Tudor, N.M. White, Energy harvesting vibration sources for microsystems applications, *Measurement Science and Technology* 17 (2006) 175–195.

[4] C.R. Saha, T. O'Donnell, N. Wang, P. McCloskey, Electromagnetic generator for harvesting energy from human motion, *Sensors and Actuators A* 147 (1) (2008) 248–253.

[5] T. von Buren, G. Troster, Design and optimization of a linear vibration-driven electromagnetic micro-power generator, *Sensors and Actuators A* 135 (2007) 765–775.

[6] S. Kulkarni, E. Koukharenko, R. Torah, J. Tudor, Design, fabrication and test of integrated macro-scale vibration-based electromagnetic generator, *Sensors and Actuators A* 145–146 (2008) 336–342.

[7] I. Sari, T. Balkan, H. Kulah, An electromagnetic micro power generator for wideband environmental vibrations, *Sensors and Actuators A* 145–146 (2008) 405–413.

[8] S.M. Shahruz, Design of mechanical band-pass filters for energy scavenging, *Journal of Sound and Vibration* 292 (3–5) (2006) 987–998.

[9] S.M. Shahruz, Limits of performance of mechanical band-pass filters used in energy scavenging, *Journal of Sound and Vibration* 293 (1–2) (2006) 449–461.

[10] C.B. Williams, R.B. Yates, Analysis of a microgenerator for microsystems, in: *Proceedings of the 8th International Conference on Solid-state Sensors and Actuators*, Stockholm, Sweden, Eurosensors IX, 1995, p. 87-B4.

[11] L.C. Rome, L. Flynn, E.M. Goldman, T.D. Yoo, Generating electricity while walking with loads, *Science* 309 (2005) 1725–1728.

[12] B.P. Mann, N.D. Sims, Energy harvesting from the nonlinear oscillations of magnetic levitation, *Journal of Sound and Vibration* 319 (2009) 515–530.

[13] E.S. Leland, P.K. Wright, Resonance tuning of piezoelectric vibration energy scavenging generators using compressive axial load, *Smart Material and Structures* 15 (2006) 1413–1420.

[14] K.W. Yung, P.B. Landecker, D.D. Villani, An analytical solution for the force between two magnetic dipoles, *Magnetic and Electrical Separation* 9 (1998) 39–52.

[15] P.B. Landecker, D.D. Villani, K.W. Yung, An analytical solution for the torque between two magnetic dipoles, *Magnetic and Electrical Separation* 10 (1999) 29–33.

[16] E.P. Furlani, *Permanent Magnet and Electromechanical Devices*, first ed., Academic Press, New York, 2001.

[17] J. Vanderlinde, *Classical Electromagnetic Theory*, second ed., Springer, Dordrecht, The Netherlands, 2004.

[18] A.H. Nayfeh, D.T. Mook, *Nonlinear Oscillations*, Wiley, New York, 1979.

[19] B.P. Mann, Energy criterion for potential well escapes in a bistable magnetic pendulum, *Journal of Sound and Vibration* 323 (2009) 864–876.

[20] J. Guckenheimer, P.J. Holmes, *Nonlinear Oscillations, Dynamical Systems, and Bifurcations of Vector Fields*, Springer, New York, 1983.

[21] J.A. Gottwald, L.N. Virgin, E.H. Dowell, Routes to escape from an energy well, *Journal of Sound and Vibration* 187 (1) (1995) 133–144.

[22] L.N. Virgin, *Introduction to Experimental Nonlinear Dynamics*, Cambridge University Press, Cambridge, UK, 2000.